Enhanced Thermoelectric Performance and Mechanical Property in Layered Chalcostibite CuSb1−xPbxSe2

Manojkumar Moorthy, Bhuvanesh Srinivasan, David Berthebaud, Rajasekar Parasuraman, Suresh Perumal

Enhanced thermoelectric performance and mechanical property in layered chalcostibite $CuSb_{1-x}Pb_xSe_2$

Manojkumar Moorthy[1], Bhuvanesh Srinivasan[2,3], David Berthebaud[4], Rajasekar Parasuraman[5], Althaf. R[6], and Suresh Perumal[1]*

[1]Laboratory for Energy and Advanced Devices (LEAD), Department of Physics and Nanotechnology, SRM Institute of Science and Technology, Kattankulathur, Chengalpattu 603 203, Tamilnadu, India.

[2]Department of Metallurgical and Materials Engineering, Indian Institute of Technology Madras (IIT-Madras), Chennai 600 036, India

[3]Ceramic Technologies Group-Center of Excellence in Materials and Manufacturing for Futuristic Mobility, Indian Institute of Technology Madras (IIT-Madras), Chennai, 600 036, India

[4]CNRS-Saint Gobain-NIMS, IRL 3629, LINK, National Institute for Materials Science (NIMS), 1-1 Namiki, Tsukuba 305-0044, Japan

[5]Department of Chemistry, School of Advanced Sciences, Vellore Institute of Technology (VIT), Vellore 632 014, Tamilnadu, India.

[6]Functional Materials Lab, PSG Institute of Advanced Studies, Coimbatore 641004, Tamilnadu, India

**Corresponding author E-mail:* drsureshperumal@gmail.com and sureshp4@srmist.edu.in

Abstract

In this work, the thermoelectric properties of *p*-type layered chalcostibite $CuSb_{1-x}Pb_xSe_2$ (x = 0−0.10) compounds prepared by vacuum melting reaction and uniaxial hot press, have been studied in the temperature range of 323−623 K. Further, aliovalent Pb^{2+} doping at Sb^{3+} site in $CuSbSe_2$ notably increases the hole concentration due to its acceptor nature and thereby enhances the electrical conductivity, σ. Importantly, a huge reduction in total thermal conductivity, κ_{total} has been noticed, from ~1.7 W/m.K (pristine $CuSbSe_2$) to ~0.72 W/m.K at 323 K for $CuSb_{0.90}Pb_{0.10}Se_2$ owing to increased phonon scattering from the introduced point defects and mass-difference between Pb and Sb. As a result, the thermoelectric figure of merit, *z*T has been enhanced to ~0.27 at 623 K for the composition of $CuSb_{0.90}Pb_{0.10}Se_2$, which is three-fold higher than that of the undoped $CuSbSe_2$ and the hardness value achieved to be ~125.54 Hv, which is significantly higher than the most of the state-of-the-art materials, reflecting to be an efficient thermoelectric material for intermediate temperature.

Keywords: $CuSbSe_2$, *p*-type semiconductor, aliovalent doping, point defect scattering, high figure of merit (*z*T)

1. Introduction

The increase in global energy needs and environmental pollution demands urgent requirement for alternative energy generation technologies. Recently, thermoelectric (TE) technology has gained more attention due to its role as a power generator that utilizes waste heat to generate electricity without involving any moving parts and with no release of toxic gases. However, this green energy technology is still constricted due to the low heat-to-electricity conversion efficiency (η_{TE}), which is determined by the dimensionless figure of merit, zT of an individual *p*-and *n*-type TE material.[1] In general, the η_{TE} of TE devices has a linear relationship with the dimensionless figure of merit, given by the relation, $zT = S^2\sigma T/(\kappa_{ele}+\kappa_{latt})$, where σ, S, T, $\kappa_{ele,}$ and κ_{latt} are the electrical conductivity, the Seebeck coefficient, the absolute temperature and the electronic and lattice thermal conductivity, respectively. Moreover, improving the zT would increase the η_{TE}, which is very challenging as TE parameters (σ, S, and κ) are interdependent in nature. In this regard, many distinct strategies, such as resonant state formation,[2] sub-bands convergence,[3] minority energy filtering,[4] nano-structuring,[5] phonon scattering by nano/meso precipitates,[6] grain boundary engineering,[7,8] and so on, have been employed in order to decouple the electronic and thermal transport and for designing high-performance TE materials. Unfortunately, most state-of-the-art TE materials, such as Bi_2Te_3,[9] PbTe,[10] GeTe,[11] and SnSe,[12] are relatively toxic and consist of expensive constituent elements, even though they exhibit a notably large thermoelectric performance and, thereby, conversion efficiency. Hence, the necessity of low-cost and eco-friendly TE material with good structural, thermal, and mechanical property remains challenging in TE research.

In this context, the layered and quasi-layered materials belong to a class that possesses electron conduction (*EC*), and electron insulating (*EI*) units that have shown an intrinsically low thermal conductivity. For instance, materials belonging to such category, especially, SnSe,[13] Bi_2Te_3,[14] In_4Se_3,[15] GeSe,[16] $Cu_2CdSnSe_4$,[17] and BiCuSeO,[18] are well-known for their superior thermoelectric performance. Additionally, the *n*- and *p*-type eco-friendly and cost-effective I-III-VI_2 class of materials, such as $CuFeS_2$[19,20] and $CuFeSe_2$,[21] have shown great attention due to their considerably high thermoelectric performance. Alternatively, these kinds of materials have led to the discovery of multicomponent materials for exploring their thermoelectric performance. In this context, among I-V-VI_2 group compounds, *p*-type chalcostibite $CuSbSe_2$ has recently gained more attention due to its low-cost, earth-abundant elements and a 2D layered honeycomb structure, which crystallizes into an orthorhombic structure (space group: *Pnma*), as seen in Figure 1(a).[22] Additionally, a six-membered ring of Sb_2CuSe_3 and $SbCu_2Se_3$

leads to a lower thermal conductivity due to the van der Waals gap (VDW) between $CuSbSe_2$ layers. Pristine $CuSbSe_2$ exhibits a direct bandgap, E_g of 1.05 eV, low carrier concentration (n = ~10^{18}/cm^3), high Seebeck coefficient of 535 μV/K at 625 K, and low thermal conductivity, κ of ~ 0.38 W/m.K at 625 K,[22] with electrical conductivity, σ ~400 S/m at 300 K,[23, 24] making it to be a suitable material for intermediate-temperature thermoelectric applications. Further, the apparent reason for such a high Seebeck coefficient is attributed to the presence of flat valence bands closer to the Fermi level (E_F) and degenerate at Z point (0, 0, ½), which leads to high effective mass m^*=2.05m_0, confirmed by the first principle DFT calculation.[25] Despite the fact being a cost-effective TE material, a lack of detailed study inhibits the ascension of its performance. Earlier work on the low-temperature study of $CuSbSe_2$ by aliovalent doping prepared by the vacuum melting method resulted in an enhanced zT of 0.0041 at 300 K for $CuTi_{0.02}Sb_{0.98}Se_2$, due to an increase in electrical conductivity and a decrease in thermal conductivity.[26] Further, mechanical alloying of $CuSbSe_2$ has resulted in a zT ~ 0.41 at 623 K due to the obtained large Seebeck coefficient (~400 μV/K) and very low thermal conductivity (~ 0.37 W/mK).[27] Nano-composite of $CuSbSe_2$-2mol.%$PtTe_2$ synthesized by wet chemical process has shown the maximum zT of ~0.5 at 673 K.[28] Moreover, $SrOCuSbSe_2$ prepared by the traditional melting salt method has seen to persist the highest zT of 0.22 at 850 K due to a high Seebeck coefficient of ~500 μV/K at 800 K and lower lattice thermal conductivity through Sb lone pair electrons and EI unit of SrO layer intercalation.[22] Further, Cd^{2+} doping at Sb^{3+} site has also exhibited a notably high zT of ~0.55 at 675 K for $CuSb_{0.98}Cd_{0.02}Se_2$, owing to an increased carrier concentration of ~3 x 10^{18} /cm^3 and thereby enhanced electrical conductivity of ~344 S/m with lower thermal conductivity of 0.76 W/mK at 300 K through enhanced phonon scattering.[24] The creation of Sb vacancies in $CuSbSe_2$ has recently improved the thermoelectric performance *via* an increase in hole concentration (24.1 x 10^{18} /cm^3) and reduced thermal conductivity, heading to the maximum zT of 0.50 at 673 K.[23] In this context, in $CuSbSe_2$, the VDW gaps induced low thermal conductivity (κ), and the inherent high Seebeck coefficient (S) can be utilized to achieve high thermoelectric performance only if the carrier concentration is optimized by the suitable dopants.

Herein, we have successfully synthesized $CuSb_{1-x}Pb_xSe_2$ (x = 0 – 0.10) samples using vacuum melting followed by induction-assisted uni-axial hotpress. Powder X-ray diffraction (P-XRD) pattern and high-resolution scanning electron microscope (HR-SEM) confirm the phase purity and microstructures with the elemental composition of as-synthesized $CuSb_{1-x}Pb_xSe_2$ compounds, respectively. Moreover, as Pb concentration increases, the bandgap

is reduced from ~1.04 eV (pristine $CuSbSe_2$) to ~0.84 eV for the composition of $CuSb_{0.90}Pb_{0.10}Se_2$, where Pb^{2+} at Sb^{3+} site acts as an acceptor and increases the carrier concentration to 16.7 x 10^{18} /cm^3 and thereby the electrical conductivity. Further, the electronic states of Cu^{1+}, Sb^{3+}, Pb^{2+}, and Se^{2-} in $CuSb_{1-x}Pb_xSe_2$ were confirmed through XPS analysis. In addition, an enhanced phonon scattering from the combination of mass-fluctuation and point defects leads to the ultra-low thermal conductivity of ~0.72 W/mK at 323 K for $CuSb_{0.90}Pb_{0.10}Se_2$. Overall, the maximum figure of merit, zT of ~0.27 at 623 K is achieved for the composition of $CuSb_{0.90}Pb_{0.10}Se_2$, which is in fact 3 times higher than that of the pristine $CuSbSe_2$.

2. Experimental details

Sample Preparation: Polycrystalline $CuSb_{1-x}Pb_xSe_2$ (x = 0.00, 0.02, 0.05, and 0.10) samples were prepared by weighing with respective stoichiometry using high pure elements of Cu (shots, 99.999%, Alfa Aesar), Sb (shots, 99.999%, Alfa Aesar) and Pb (shots, 99.9999%, Alfa Aesar) and Se (shots,99.99%, Alfa Aesar) and then transferred to quartz ampoule and sealed them under a vacuum level of 10^{-5} mbar. The sealed ampoules were slowly heated up to 1073 K in 10 h, soaked for 10 h, and then slowly cooled down to room temperature in 10 h using a programmable furnace. The ingots thus obtained were pulverized to powders and then compacted to the bulk pellet with the help of induction hot-press at a temperature of 653 K under a pressure of 45 MPa. The pellets were directly used for thermal conductivity measurements and were then cut into rectangular bars for the electrical conductivity and Seebeck coefficient measurements.

Material Characterization: The phase structure and solid solubility of $CuSb_{1-x}Pb_xSe_2$ (x= 0-0.10) samples were analyzed using powder X-ray diffraction (XRD), BRUKER USA D8 Advance, Davinci with a Cu-Kα radiation in the wavelength, λ = 1.5406 Å. Further, the lattice parameters were calculated by the profile fitting from Rietveld refinement using GSAS-II software. Further, Raman vibrational spectra of all the samples were recorded using micro-Raman spectrometer, HORIBA LABRAM HR Evolution excited with a 633 nm laser at room temperature equipped with an auto-cooled CCD detector. The sample's room temperature optical bandgap was obtained from the diffused reflectance measurement using a SHIMADZU, UV 3600 PLUS instrument recorded from 200 to 1800 cm^{-1} with 2 cm^{-1} resolutions. Further, the Kubelka-Munk equation: $\alpha/\Lambda=(1-R)^2/(2R)$ was used to calculate the absorption (α/Λ) from the reflectance data, where R is the reflectance, α and Λ are the absorption and scattering

coefficient, respectively.

The microstructures with back-scattered electron (BSE) mode, phase composition, and fracture morphology in $CuSb_{1-x}Pb_xSe_2$ (x = 0 and 0.10) samples were clearly examined using the high-resolution scanning electron microscopy (HR-SEM) equipped with EDS using Thermo scientific Apreo S, USA. In addition, X-ray photoelectron spectroscopy (XPS) analyses were carried out to evaluate the existence of elements and the oxidation states of Cu, Sb, Pb, and Se in $CuSb_{1-x}Pb_xSe_2$ with Shimadzu ESCA-3400 (Kyoto, Japan) using monochromatic Mg-Kα source (1253.6 eV) operating at 10 kV and 10 mA.

Thermoelectric measurements: The room temperature Hall measurements were taken with van der Pauw geometry using the HMS 5300 Hall System. The electrical conductivity (σ) and Seebeck coefficient (S) were measured simultaneously under a partial He atmosphere in the temperature range of 323-623 K using a ULVAC-RIKO ZEM-3 instrument system and the rectangular bar-shaped samples with dimensions of ~2 x ~2 x ~8 mm^3 were used for the measurements.

The thermal diffusivity (D) of all samples in the 323-623 K temperature range was directly measured using the laser flash analyzer (LFA), Netzsch LFA 457. Further, the total thermal conductivity (κ_{total}) was calculated using the relation $\kappa_{total} = DC_pd$, where D is the thermal diffusivity (mm^2/s), C_p is the specific heat capacity (J/g/K), and d is the density of the samples. The coin-shaped samples with ~10 mm diameter and ~2 mm thickness were used in all of the measurements. Here, the temperature-dependent specific heat capacity (C_p) was derived from LFA measurement, where pyroceram was used as a reference material, which coincides well with the Dulong-Petit C_p value. The Archimedes method was used to measure the sample's density, where all the samples showed above 92 ± 2% of X-ray theoretical density. Moreover, the measurements uncertainties of electrical conductivity, Seebeck coefficient, and thermal conductivity are ± 2 %, ± 3 %, and ± 5 %, respectively.

Hardness measurement: The hardness of $CuSb_{1-x}Pb_xSe_2$ (x= 0 and 0.10) samples were examined by performing a nano-indentation experiment using the Nios Scanning Nanohardness tester. Here, a load of 80 mN was applied to the samples with a loading and unloading time of 5 s for a holding time of 2 s. The hardness of the material is calculated from the relation, $H = \frac{P_{max}}{A_c}$, where P_{max} is the maximum load applied, and A_c is the contact area at maximum load.

3. Results and Discussion:

The powder X-ray diffraction patterns of as-synthesized $CuSb_{1-x}Pb_xSe_2$ (x = 0-0.10) samples are shown in Figure 1(b). The Bragg's peak with high intensity is observed at the angle, 2θ of 28.73º for all the samples, corresponding to the plane of (013). All the patterns of $CuSb_{1-x}Pb_xSe_2$ can be indexed with an orthorhombic crystal structure with a space group of *Pnma* and matched well with the ICSD no: 418754. Further, as Pb concentration increases, Bragg's peaks shift towards the lower angle side due to the higher atomic radius of Pb (*r(Pb)* = 1.75 Å) than that of Sb (*r(Sb)* = 1.59 Å), which follows Vegard's law for the solid solubility of Pb at Sb site in $CuSbSe_2$. The profile fitting of Rietveld refinement was done to obtain the lattice parameters (refer Figure S1 (a), (b), and (c), Supporting Information). As Pb content increases, the lattice parameter of all the samples increases, as shown in Table 1. Particularly, the lattice parameters were calculated as a = 6.2965(2) Å, b = 3.9755(3) Å, and c = 14.9675(5) Å for pristine $CuSbSe_2$ which increases to a = 6.30729(7) Å, b = 3.9863(2) Å, and c = 15.0119(4) Å for the composition of $CuSb_{0.90}Pb_{0.10}Se_2$. Moreover, the presence of small content of Cu_3SbSe_3 was also seen as a secondary phase upon Pb doping in $CuSbSe_2$, as denoted in Figure 1(b). Further, the phase content of Cu_3SbSe_3 in as-synthesized 10 mol.% of Pb doped $CuSbSe_2$ powders has been calculated as the weight fraction of ~9.1 from the Rietveld refinement, refer Figure S1(b), Supporting Information.

Figure 1(c) presents the Raman vibration spectra of $CuSb_{1-x}Pb_xSe_2$ (x = 0-0.10) samples in the range of 100-600 cm^{-1}. The vibration mode with high intensity is seen around 211 cm^{-1}, and other vibration modes are observed at 140 cm^{-1}, 186 cm^{-1}, 251 cm^{-1}, and 449 cm^{-1} for all the samples. The representation of vibration modes in $CuSbSe_2$ are given as,[29-32]

$$M = 8A_g + 4A_u + 4B_{1g} + 8B_{1u} + 8B_{2g} + 4B_{2u} + 4B_{3g} + 8B_{3u}$$

The Raman active modes are A_g, B_{1g}, B_{2g}, and B_{3g}, where the high intense peak at 211 cm^{-1} corresponds to the A_g mode of the $CuSbSe_2$ phase, which is singly degenerate with symmetry about the inversion center. At the same time, the peak at 140 cm^{-1} corresponds to B_{3g} mode. Further, peaks appear at 186 cm^{-1}, and 251 cm^{-1} can be assigned to binary Sb_2Se_3 or ternary Cu_3SbSe_3, which can be attributed to secondary phase modes as it is very difficult to distinguish the vibrations between those two phases.[33] The vibration mode around 259 cm^{-1}, a characteristic mode of Cu-Se, has not been observed. Moreover, from the Raman spectra, the vibration mode at 186 cm^{-1} corresponds to Cu_3SbSe_3 as the secondary phase,[32] supporting the XRD pattern.

Figure 1(d) illustrates the optical absorption spectra of $CuSb_{1-x}Pb_xSe_2$ (x = 0-0.10) samples in the energy range of 0.8-2.0 eV, depicted as α/Λ *vs.* E_g (eV) using Kubelka-Munk

relation. The direct optical bandgap of pure $CuSbSe_2$ is measured as 1.04 eV, which agrees well with the previous reports. [25,34,35] Typically, the partial density of the states of $CuSbSe_2$ from the first-principle studies reveals that Cu-3d and Se-4p orbitals form at the top of the valence bands and Sb-5p and Se-4p orbitals lie at the bottom of the conduction bands, wherein the conduction band possesses Sb-5p driven p-orbital character.[23,27] As the aliovalent dopant of Pb^{2+} content increases at Sb^{3+} site, confirmed from XPS (discussed in later section) in $CuSbSe_2$, the obtained optical bandgap is noticed to reduce significantly. Particularly, the bandgap is decreased from ~1.04 eV (pristine $CuSbSe_2$) to ~0.84 eV for the composition of $CuSb_{0.90}Pb_{0.10}Se_2$. This notable reduction in the bandgap is due to the formation of Pb states above the valence band in $CuSbSe_2$ upon increase in Pb content as the electronegativity of Pb (χ_{Pb} ~2.33 in Pauling scale) is lesser than Se (χ_{Se} ~2.55) and higher than that of Sb (χ_{Sb} ~2.05). Moreover, the aliovalent dopant of Pb-induced impurity states above the valence band causes the reduction in the bandgap of $CuSbSe_2$, which is majorly responsible for the increase in carrier concentration (n_p) and, thereby, electrical conductivity.

Backscattered electron (BSE) micrographs and EDS spectra are recorded using HR-SEM to examine the phase homogeneity throughout the sample, and elemental compositions, respectively. Figure 2(a-f) and Figure 2(g-l) depict the BSE micrographs with EDX spectra of individual elements for $CuSb_{1-x}Pb_xSe_2$ (x = 0 and 0.10) samples. Particularly, Figure 2(a) illustrates the BSE micrograph of the polished surface of pure $CuSbSe_2$ with no notable trace of secondary phases, and Figure 2(b)-(d) depicts the elemental mapping of Cu, Sb, and Se, respectively, where chemical homogeneity and existence of elements was clearly distinguishable. A region EDS spectrum of pristine $CuSbSe_2$ reveals the stoichiometric composition to be in the ratio of 1:1.06:1.92, as presented in Figure 2(e). Moreover, relative compaction of grains in $CuSbSe_2$ without voids are precisely seen in the fractured micrograph, refer Figure 2(f). Similarly, Figure 2(g) illustrates the BSE micrograph of $CuSb_{0.90}Pb_{0.10}Se_2$ and Figure 2(h)-(k) represents the EDS elemental mapping of Cu, Sb, Se, and Pb, respectively. The EDS spectra evidences the presence of Pb in $CuSb_{0.90}Pb_{0.10}Se_2$ sample (refer Figure S2, Supporting Information), and the stoichiometric composition ratio was observed to be 1:0.91:0.095:1.75 for the corresponding elements of Cu, Sb, Pb, and Se, respectively. Moreover, the elemental composition of $CuSbSe_2$ and $CuSb_{0.90}Pb_{0.10}Se_2$ measured from EDS is listed in Table S1, Supporting Information. Additionally, the grains in sintered pellet are densely packed without noticeable voids, which is observed from the fractured surface of $CuSb_{0.90}Pb_{0.10}Se_2$, as seen in Figure 2(l), confirming that pellets are effectively compacted.

Figure 3 presents the survey, and core spectra of $CuSb_{1-x}Pb_xSe_2$ (x = 0 and 0.10) samples using X-ray photoelectron spectroscopy (XPS), where the existence of elements and oxidation states of Cu, Sb, Pb, and Se were examined. Figure 3(a) depicts the survey spectrum of $CuSbSe_2$, which confirms the presence of Cu, Sb, and Se, whereas the survey spectrum of $CuSb_{0.90}Pb_{0.10}Se_2$, see Figure 3(b) evidences the existence of doped Pb. Moreover, the Cu-2p core spectra is presented in Figure 3(c), where the $2p_{3/2}$ and $2p_{1/2}$ peaks are positioned at 932 eV and 952 eV, respectively, with spin-orbit splitting (SOS) of 20 eV in $CuSbSe_2$, whereas the peaks are observed at 932.6 eV and 952.6 eV with SOS of 20 eV in $CuSb_{0.90}Pb_{0.10}Se_2$, confirming that Cu possesses an oxidation state of +1 in both the samples, consistent with the literature.[36] Similarly, the core level spectrum of Sb is shown in Figure 3(d), where the peaks of $3d_{5/2}$ and $3d_{3/2}$ are obtained at binding energies of 531 eV and 540 eV with SOS of 9 eV for $CuSb_{0.90}Pb_{0.10}Se_2$, matching with literature.[37] The Se core spectrum is presented in Figure 3(e), wherein the peaks are seen at the binding energies of 53.8 eV and 55.08 eV with SOS of 1.28 eV in $CuSbSe_2$ and peaks at 53.7 eV and 54.9 eV with SOS of 1.2 eV, in $CuSb_{0.90}Pb_{0.10}Se_2$, ascribed to the existence of Se^{2-} ions in the $CuSb_{1-x}Pb_xSe_2$ (x = 0 and 0.10) samples.[36] Moreover, the presence of doped Pb in the $CuSb_{0.90}Pb_{0.10}Se_2$ was rechecked with the core spectrum of Pb spectra, as presented in Figure 3(f), which depicts that the peaks occur at binding energies of 138.4 eV and 143.3 eV with SOS of 3.9 eV, confirming the +2 oxidation state of Pb, in correlation with literature.[38] It is noteworthy that aliovalent Pb^{2+} replaces Sb^{3+} ions and performs as an acceptor, which increases the hole concentration, n_p, and is responsible for the bandgap reduction, coincident with optical bandgap measurement (refer to Figure 1(c)).

4. Thermoelectric properties

Figure 4(a) presents the temperature-dependent electrical conductivity (σ) of $CuSb_{1-x}Pb_xSe_2$ (x = 0-0.10) samples in the temperature range of 323-623 K. The σ of all the samples decreases with an increase in temperature, which dictates the heavily doped semiconductor behavior. Typically, the σ of pristine $CuSbSe_2$ is 243 S/m at room temperature, which decreases to 233 S/m at 573 K. As Pb content increases in $CuSbSe_2$, the σ gets increased throughout the measured temperature range. To be specific, the σ starts increasing at 323 K as ~243 S/m, 895 S/m, 1600 S/m, and 1876 S/m for the compositions of $CuSbSe_2$, $CuSb_{0.98}Pb_{0.02}Se_2$, $CuSb_{0.95}Pb_{0.05}Se_2$, and $CuSb_{0.90}Pb_{0.10}Se_2$, respectively. Moreover, the σ value decreases from 1876 S/m at 323 K to 1426 S/m at 623 K for the composition of $CuSb_{0.90}Pb_{0.10}Se_2$. Overall, a maximum electrical conductivity value is observed for 10 mol.% Pb doped $CuSbSe_2$. To understand the σ of $CuSb_{1-x}Pb_xSe_2$ (x= 0-0.10) samples, the room-

temperature Hall measurement (See Figure S1(d), Supporting Information) has been performed at room temperature with a constant magnetic field of 0.5 T. The measured carrier concentration, n_p of $CuSbSe_2$ is ~1.12 x 10^{18} /cm^3 at 300 K which increases upon Pb doping as ~2.23 x 10^{18} /cm^3, ~5.86 x 10^{18} /cm^3 and ~16.7x10^{18} /cm^3 for the respective compositions of $CuSb_{0.98}Pb_{0.02}Se_2$, $CuSb_{0.95}Pb_{0.05}Se_2$, and $CuSb_{0.90}Pb_{0.10}Se_2$, (listed in the Table 2). It is clear that as Pb content increases, the n_p values of all the samples increases, which is mainly responsible for the obtained enhancement in the σ. This rise in n_p is due to doping of Pb^{2+} at the Sb^{3+} site of $CuSbSe_2$ that behaves as an acceptor and generates more holes. Further, the hole motilities (μ_H) were calculated at 300 K for $CuSb_{1-x}Pb_xSe_2$ (x= 0-0.10) samples, which are 161 $cm^2V^{-1}s^{-1}$, 30.4 $cm^2V^{-1}s^{-1}$, 25.6 $cm^2V^{-1}s^{-1,}$ and 14 $cm^2V^{-1}s^{-1}$, respectively. It is noteworthy that the μ_H significantly reduces as Pb content increases and is relatively higher for pristine $CuSbSe_2$ than Pb-doped samples (See Figure S1(d), Supporting Information) due to alloying effect.

The temperature-dependent Seebeck coefficient, S of $CuSb_{1-x}Pb_xSe_2$ (x = 0-0.10) samples in the temperature range of 323-623 K are presented in Figure 4(b). The positive value of S for all the samples in the measured temperature range confirms the *p*-type conduction in the system, suggesting that the holes play an essential role for thermoelectric transport rather than electrons. The S of $CuSbSe_2$ is ~451 µV/K at 323 K, and it increases to ~477 µV/K at 623 K. However, the S of $CuSb_{1-x}Pb_xSe_2$ samples is subsequently decreased due to the significant increase in carrier concentration. Particularly, the S of $CuSbSe_2$ is ~451 µV/K at 323 K which reduces to ~394 µV/K, ~326 µV/K and ~256 µV/K for the compositions of $CuSb_{0.98}Pb_{0.02}Se_2$, $CuSb_{0.95}Pb_{0.05}Se_2$, and $CuSb_{0.90}Pb_{0.10}Se_2$, respectively. Moreover, the sample of $CuSb_{0.98}Pb_{0.10}Se_2$ exhibits the S of ~256 µV/K, which increases with temperature and reaches the maximum value of ~331 µV/K at 623 K.

The temperature-dependent power factor ($S^2\sigma$) of $CuSb_{1-x}Pb_xSe_2$ (x= 0-0.10) samples are presented in Figure 4(c). The room temperature $S^2\sigma$ of pure $CuSbSe_2$ is ~0.049 mW/mK^2, which rises to a maximum of ~0.08 mW/mK^2 at 623 K. Particularly, the maximum $S^2\sigma$ value is observed for the 5 mol.% Pb doped $CuSbSe_2$ sample as ~0.170 mW/mK^2 at 323 K rises to a maximum value of ~0.185 mW/mK^2 at 623 K. Figure 4(d) presents the comparison plot of $S^2\sigma$ and σ as a bar diagram with the previous report, where the sample of $CuSb_{0.90}Pb_{0.10}Se_2$ shows notably large value, about 54% higher than that of previous reports [22, 24, 28] and electrical conductivity, σ is significantly higher than the earlier reports.[22, 24, 28]

The total thermal conductivity, κ_{total} of $CuSb_{1-x}Pb_xSe_2$ (x = 0-0.10) samples was estimated in the temperature range of 323–623 K, as seen in Figure 5(a), using the relation,

$\kappa_{total} = \rho.C_p.D$, where D is the thermal diffusivity, C_p is the specific heat capacity, and ρ is the density of the sample. The κ_{total} of all the samples decreases with a rise in temperature, as seen in typical solids. At 323 K, pristine $CuSbSe_2$ possesses the κ_{total} of ~1.69 W/mK, and it starts decreasing with rise in temperature and attains the minimum value of ~0.55 W/mK at 623 K. As Pb concentration increases in $CuSbSe_2$, the κ_{total} is considerably reduced around room temperature and follows the measured temperature region overall. Particularly, the κ_{total} of $CuSbSe_2$ is ~1.69 W/mK and it substantially reduces to ~1.07 W/mK, ~0.9 W/mK, and ~0.72 W/m.K for the compositions of $CuSb_{0.98}Pb_{0.02}Se_2$, $CuSb_{0.95}Pb_{0.05}Se_2$, and $CuSb_{0.90}Pb_{0.10}Se_2$, respectively. This significant reduction upon doping of Pb in $CuSbSe_2$ is due to mass-fluctuation and point defects driven phonons scattering, discussed in the later section. Moreover, a minimum κ_{total} of ~0.72 W/mK at 323 K is observed for the composition of $CuSb_{0.90}Pb_{0.10}Se_2$, which further reduces with increase in temperature and reaches to ~0.36 W/mK at 623 K.

The electronic thermal conductivity, κ_{el} was calculated and displayed in the Figure 5(b). The κ_{el} of all the samples were calculated using the Wiedemann-Franz law, $\kappa_{el} = \sigma \cdot L \cdot T$, where L represents the Lorentz number (L = 2.44 x 10^{-8} WΩ/K^2 for degenerate semiconductors and metals), and it is calculated from the temperature-dependent experimental Seebeck co-efficient data (S *vs.* T) by estimating the reduced chemical potential using an SPB model from the following equation,[39–41]

$$L = \left(\frac{k_B}{e}\right)^2 \cdot \left\{\frac{3F_0(\eta)F_2(\eta) - 4F_1(\eta)^2}{F_0(\eta)^2}\right\} \quad \ldots(1)$$

where k_B, η *and* e represent the Boltzmann constant, the reduced chemical potential, and the charge of an electron, respectively. The L values were found as 1.50 x 10^{-8} WΩ/K^2, 1.51 x 10^{-8} WΩ/K^2, 1.53 x 10^{-8} WΩ/K^2, and 1.56 x 10^{-8} WΩ/K^2 for $CuSb_{1-x}Pb_xSe_2$ samples (x = 0.0, 0.2, 0.5, and 0.10), respectively. The κ_{el} of $CuSb_{1-x}Pb_xSe_2$ (x = 0-0.10) samples is notably low when compared to the κ_{total}. Moreover, the κ_{el} of $CuSbSe_2$ starts increasing upon rise in Pb content due to an increase in hole concentration, and it rises with an increase in temperature. Particularly, the κ_{el} of $CuSbSe_2$ is ~0.001 W/mK at 323 K which increases as 0.003 W/mK, 0.006 W/mK and 0.009 W/mK for the composition of $CuSb_{0.98}Pb_{0.02}Se_2$, $CuSb_{0.95}Pb_{0.05}Se_2$, and $CuSb_{0.90}Pb_{0.10}Se_2$, respectively.

The lattice thermal conductivity, κ_{latt} of $CuSb_{1-x}Pb_xSe_2$ (x = 0-0.10) samples was obtained by subtracting the κ_{el}, from the κ_{total} and is plotted in Figure 5(c). The κ_{latt} of $CuSbSe_2$ follows the relation of $\kappa_{latt} \propto T^{-1}$ showing the domination of the Umklapp (U) process.[24] Moreover, the κ_{latt} of all the samples decreases with an increase in temperature. Typically, the

κ_{latt} of $CuSb_{1-x}Pb_xSe_2$ is ~1.69 W/mK at 323 K, and it reduces to ~0.59 W/mK at 623 K. Upon Pb doping, the κ_{latt} of $CuSb_{1-x}Pb_xSe_2$ is seen to reduce significantly due to mass-fluctuation and point defects driven phonon scattering.[24] Particularly, the κ_{latt} of $CuSbSe_2$ is ~1.69 W/mK at 323 K and it considerably reduces as ~1.07 W/mK,~ 0.88 W/mK and ~0.71 W/mK for the composition of $CuSb_{0.98}Pb_{0.02}Se_2$, $CuSb_{0.95}Pb_{0.05}Se_2$, and $CuSb_{0.90}Pb_{0.10}Se_2$, respectively. It is important to note that the composition of $CuSb_{0.90}Pb_{0.10}Se_2$ exhibits the κ_{latt} of ~0.71 W/mK at 323 K, that notably reduces to ~0.36 W/mK at 623 K, approaching the theoretically minimum κ_{latt}.

To unveil the underlying mechanism behind the huge reduction in the κ_{latt}, the Debye model was adopted to calculate the κ_{latt} with the following relations,[42–45]

$$\kappa_{latt} = \frac{4\pi k_B^4 T^3}{\nu h^3} \int_0^{\theta_D/T} \tau_T \frac{z^4 \exp(z)}{[\exp(z)-1]^2} dz \quad \ldots(2)$$

where θ_D, ν , τ_T , and z are the Debye temperature, mean sound speed, total phonon relaxation time, and the reduced phonon frequency. Based on the Matthiessen rule, one can express τ_T as,[46]

$$\tau_T{}^{-1} = \tau_{PD}{}^{-1} + \tau_U{}^{-1} + \tau_N{}^{-1} + \tau_B{}^{-1} + \tau_D{}^{-1} \quad \ldots(3)$$

Where $\tau_{PD}{}^{-1}, \tau_U{}^{-1}, \tau_N{}^{-1}, \tau_B{}^{-1}\ and \tau_D{}^{-1}$ are scattering relaxation times of point defects, Umklapp-process, nano-inclusions, boundaries/interfaces, and dislocations. The probability of phonon scattering for pure $CuSbSe_2$ with Umklapp scattering as the dominant mechanism $\tau_U{}^{-1}$ can be written as,

$$\tau_U{}^{-1} = B\omega^2 T \exp\left(-\frac{\theta_D}{3T}\right) \quad \ldots(4)$$

In the relation, B is the factor of the Umklapp (U) process, and κ_{latt} was calculated using equations (2) and (4). Here, the U process is dominant for pristine $CuSbSe_2$, whereas, for Pb-doped samples, the point defects play a vital role in the phonon scattering and reduce the κ_{latt} significantly, where the fitted curves are indicated as dashed lines in Figure 5 (c).

The total scattering rate expression for $CuSb_{1-x}Pb_xSe_2$ (x = 0-0.10) samples is given by,

$$\tau^{-1} = \tau_{PD}{}^{-1} + \tau_U{}^{-1} = A\omega^4 + B\omega^2 T \exp\left(-\frac{\theta_D}{3T}\right) \quad \ldots(5)$$

Where A is the simplified point defect parameter. Notably, the U+PD process contributes to the reduction in thermal conductivity for $CuSb_{1-x}Pb_xSe_2$ (x = 0-0.10) samples (as seen in the Figure 5(c), indicating that the phonons are significantly scattered by the point defects generated by doping of Pb^{2+} at Sb^{3+} site in $CuSbSe_2$ and by the mass difference between Pb and Sb with the meso-scale scattering from Cu_3SbSe_3 secondary phase.[24] For this calculation, θ_D, and ν were

fixed as 56 K and 1786 ms^{-1}, respectively.[24, 47] The magnitudes of A and B were obtained *via* the Debye approximation presented in Table 1.

Further, the theoretical minimum lattice thermal conductivity $(\kappa_{latt})_{min}$ of $CuSbSe_2$ is calculated from the following relation,

$$(\kappa_{latt})\min = \frac{1}{2}\left(\frac{\pi}{6}\right)^{\frac{1}{3}} kV^{\frac{-2}{3}}(2v_t + v_l) \quad \ldots (6)$$

Where V, v_t, and v_l are the unit cell volume, the transverse sound velocity, and longitudinal sound velocity, respectively. Utilizing the sound velocity data of $CuSbSe_2$,[47] the minimum lattice thermal conductivity $(\kappa_{latt})_{min}$ is estimated as ~0.36 W/mK, see the dotted line in Figure 5(c). Importantly, the experimentally observed κ_{min} of $CuSb_{0.90}Pb_{0.10}Se_2$ is ~0.36 W/mK, which is indeed close to the calculated minimum κ_{latt}.

The temperature dependence of *z*T of $CuSb_{1-x}Pb_xSe_2$ (x = 0, 0.02, 0.05, and 0.10) samples are shown in Figure 6(a). All the samples exhibit a similar increasing trend with an increase in temperature. Typically, pure $CuSbSe_2$ exhibits the *z*T of 0.001 at 323 K, increasing with temperature and reaching to ~0.09 at 623 K. Moreover, the *z*T of $CuSbSe_2$ increases upon Pb doping in the measured temperature range of 323-623 K. Particularly, the *z*T increases as 0.09, 0.15, 0.17, and 0.27 at 623 K for the compositions of $CuSbSe_2$, $CuSb_{0.98}Pb_{0.02}Se_2$, $CuSb_{0.95}Pb_{0.05}Se_2$, and $CuSb_{0.90}Pb_{0.10}Se_2$, respectively. To be specific, a maximum zT of 0.27 at 623 K is achieved for the $CuSb_{0.90}Pb_{0.10}Se_2$, which is almost three-fold higher than that of pure $CuSbSe_2$. Further, this notable improvement in zT is due to an increase in the σ via acceptor Pb-induced rise in hole concentration and a huge reduction in κ_{latt} through increased phonon scattering from mass-difference between Pb and Sb and the point defects.

Figure 6(b) compares the zT of $CuSbSe_2$ and $CuSb_{0.90}Pb_{0.10}Se_2$ with the previously reported $CuSbSe_2$-based materials, [22,23,24,27,28] where the composition of $CuSb_{0.90}Pb_{0.10}Se_2$ shows higher values when compared to the reports, [22,27,28] which can be further improved by choice of suitable dopant to bring it as an efficient thermoelectric material for intermediate temperature. The thermoelectric parameter of the carrier concentration (n_p), electrical conductivity (σ), Seebeck coefficient (*S*), total thermal conductivity (κ_{total}), and thermoelectric figure of merit (zT) of all the samples are summarized in Table 2.

6. Mechanical stability:

Apart from maximum zT, materials should exhibit high mechanical properties so as to slice them for preparing TE devices. In this concern, the nano-indentation measurement was

carried out on the pelletized $CuSb_{1-x}Pb_xSe_2$ (x= 0 and 0.10) samples to measure the hardness values, as shown in Figure 7(a). As a result, the hardness of $CuSbSe_2$ is found to be ~73.9 Hv, consistent with previous reports,[48-51] whereas the sample of $CuSb_{0.90}Pb_{0.10}Se_2$ exhibits the hardness value of 125.5 H_V, which is above ~70% higher than the pristine $CuSbSe_2$. This increase in hardness upon Pb doping in $CuSbSe_2$ is due to strong bondings produced by the heavier element of Pb with more orbitals and formed point defects.[51] Figure 7(b) compares the hardness of $CuSbSe_2$ and $CuSb_{0.90}Pb_{0.10}Se_2$ with the previously reported state-of-the-art materials,[48-51] where the composition of $CuSb_{0.90}Pb_{0.10}Se_2$ exhibits the higher value, that provides an added advantage to the use of $CuSbSe_2$-based materials as an efficient TE material.

5. Conclusion

Here, we have experimentally demonstrated the high thermoelectric performance of $CuSb_{1-x}Pb_xSe_2$ (x= 0-0.10) samples prepared by vacuum melting and inductive-assisted hot-pressing. Upon Pb doping in $CuSbSe_2$, the electrical conductivity significantly increases due to the acceptor-driven large hole concentration, whereas the Seebeck coefficient substantially reduces. Notably, a huge reduction in the thermal conductivity (κ_{total}) was observed due to increased phonon scattering *via* mass-fluctuation between Pb and Sb, and point defects created by Pb doping. As a result, a maximum thermoelectric figure of merit, zT was achieved to be ~0.27 at 623 K for the composition of $CuSb_{0.90}Pb_{0.10}Se_2$, which is three times higher than the pristine $CuSbSe_2$, justifying Pb doping as an efficient pathway to improve TE performance of $CuSbSe_2$. Additionally, a higher hardness value of ~125.54 Hv was obtained for $CuSb_{0.90}Pb_{0.10}Se_2$, which is two-fold higher than the undoped $CuSbSe_2$ and most of the state-of-the-art TE materials, showcasing it to be a promising TE material and it can be further improved upon suitable dopants and nano-structuring.

Associated content

Supporting information:

Profile fitting of Rietveld refinement for $CuSb_{1-x}Pb_xSe_2$ (x=0 and 0.10) samples, lattice parameters, and carrier concentration and mobility of $CuSb_{1-x}Pb_xSe_2$ (x = 0-0.10) samples as a function of Pb concentration. The EDX spectra of $CuSb_{0.90}Pb_{0.10}Se_2$ sample.Elemental composition table of $CuSb_{1-x}Pb_xSe_2$ (x=0 and 0.10) samples.

Declaration of Competing Interest

The authors declare that they have no known competing financial interests or personal

relationships that could have appeared to influence the work reported in this paper.

Acknowledgment
MMK would like to thank the SRM IST, India, for his research fellowship. SP wants to sincerely thank the funding agency of Science and Engineering Research Board (SERB), Govt. of India (File No. EEQ/ 2018/001365). We acknowledge Nanotechnology Research Centre (NRC), SRMIST for providing the research facilities. We acknowledge SCIF, SRMIST for high resolution scanning electron microscope (HR-SEM) facility. The authors also thank Dr. Sadhana Katlakunta, Osmania University, Hyderabad for her help in XPS measurements. The authors thank Mr. Hajeesh and Dr. Kiran Mangalampalli, SRM IST, Kattankulathur for help on the nano-indentation analysis.

References:

1. He, J.; Tritt, T. M. Advances in Thermoelectric Materials Research: Looking Back and Moving Forward. *Science* **2017**, *357* (6358), eaak9997.
2. Zhong, M.; Li, S.; Duan, H. J.; Hu, L. Bin; Yang, M.; Wang, R. Q. Effect of Impurity Resonant States on Optical and Thermoelectric Properties on the Surface of a Topological Insulator. *Sci. Rep.* **2017**, *7* (1), 1–10.
3. Pei, Y.; Shi, X.; Lalonde, A.; Wang, H.; Chen, L.; Snyder, G. J. Convergence of Electronic Bands for High Performance Bulk Thermoelectrics. *Nature* **2011**, *473* (7345), 66–69.
4. Gayner, C.; Amouyal, Y. Energy Filtering of Charge Carriers: Current Trends, Challenges, and Prospects for Thermoelectric Materials. *Adv. Funct. Mater.* **2020**, *30* (18), 1901789.
5. Hung, N. T.; Nugraha, A. R. T.; Yang, T.; Saito, R. Confinement Effect in Thermoelectric Properties of Two–Dimensional Materials. *MRS Adv.* **2020**, *5* (10), 469–479.
6. Perumal, S.; Roychowdhury, S.; Biswas, K. Reduction of Thermal Conductivity through Nanostructuring Enhances the Thermoelectric Figure of Merit in $Ge_{1-x}Bi_xTe$. *Inorg. Chem. Front.* **2016**, *3* (1), 125–132.
7. Biswas, K.; He, J.; Zhang, Q.; Wang, G.; Uher, C.; Dravid, V. P.; Kanatzidis, M. G. Strained Endotaxial Nanostructures with High Thermoelectric Figure of Merit. *Nature Chem.* **2011**, *3* (2), 160–166.
8. Biswas, K.; He, J.; Blum, I. D.; Wu, C. I.; Hogan, T. P.; Seidman, D. N.; Dravid, V. P.; Kanatzidis, M. G. High-Performance Bulk Thermoelectrics with All-Scale Hierarchical

Architectures. *Nature* **2012**, *489* (7416), 414–418.

9. Liu, R.; Tan, X.; Ren, G.; Liu, Y.; Zhou, Z.; Liu, C.; Lin, Y.; Nan, C. Enhanced Thermoelectric Performance of Te-Doped $Bi_2Se_{3-x}Te_x$ Bulks by Self-Propagating High-Temperature Synthesis. *Cryst.* **2017**, *7* (9), 257.
10. Wu, D.; Zhao, L. D.; Tong, X.; Li, W.; Wu, L.; Tan, Q.; Pei, Y.; Huang, L.; Li, J. F.; Zhu, Y.; Kanatzidis, M. G.; He, J. Superior Thermoelectric Performance in PbTe–PbS Pseudo-Binary: Extremely Low Thermal Conductivity and Modulated Carrier Concentration. *Energy Environ. Sci.* **2015**, *8* (7), 2056–2068.
11. Perumal, S.; Samanta, M.; Ghosh, T.; Shenoy, U. S.; Bohra, A. K.; Bhattacharya, S.; Singh, A.; Waghmare, U. V.; Biswas, K. Realization of High Thermoelectric Figure of Merit in GeTe by Complementary Co-Doping of Bi and In. *Joule* **2019**, *3* (10), 2565–2580.
12. Chang, C.; Wu, M.; He, D.; Pei, Y.; Wu, C. F.; Wu, X.; Yu, H.; Zhu, F.; Wang, K.; Chen, Y.; Huang, L.; Li, J. F.; He, J.; Zhao, L. D. 3D Charge and 2D Phonon Transports Leading to High Out-of-Plane ZT in *n*-type SnSe Crystals. *Science* **2018**, *360 (6390)*, 778–783.
13. Zhao, L. D.; Lo, S. H.; Zhang, Y.; Sun, H.; Tan, G.; Uher, C.; Wolverton, C.; Dravid, V. P.; Kanatzidis, M. G. Ultralow Thermal Conductivity and High Thermoelectric Figure of Merit in SnSe Crystals. *Nature* **2014**, *508 (7496)*, 373–377.
14. Poudel, B.; Hao, Q.; Ma, Y.; Lan, Y.; Minnich, A.; Yu, B.; Yan, X.; Wang, D.; Muto, A.; Vashaee, D.; Chen, X.; Liu, J.; Dresselhaus, M. S.; Chen, G.; Ren, Z. High-Thermoelectric Performance of Nanostructured Bismuth Antimony Telluride Bulk Alloys. *Science* **2008**, *320 (5876)*, 634–638.
15. Yin, X.; Liu, J. Y.; Chen, L.; Wu, L. M. High Thermoelectric Performance of In_4Se_3-Based Materials and the Influencing Factors. *Acc. Chem. Res.* **2018**, *51* (2), 240–247.
16. Hao, S.; Shi, F.; Dravid, V. P.; Kanatzidis, M. G.; Wolverton, C. Computational Prediction of High Thermoelectric Performance in Hole Doped Layered GeSe. *Chem. Mater.* **2016**, *28* (9), 3218–3226.
17. Liu, M. L.; Chen, I. W.; Huang, F. Q.; Chen, L. D. Improved Thermoelectric Properties of Cu-Doped Quaternary Chalcogenides of $Cu_2CdSnSe_4$. *Adv. Mater*. **2009**, *21*, 3808−3812.
18. Zhao, L. D.; He, J.; Berardan, D.; Lin, Y.; Li, J. F.; Nan, C. W.; Dragoe, N. BiCuSeO Oxyselenides: New Promising Thermoelectric Materials. *Energy Environ. Sci.* **2014**, *7* (9), 2900–2924.

19. Tsujii, N.; Mori, T. High thermoelectric power factor in a carrier-doped magnetic semiconductor $CuFeS_2$. *Appl. Phys. Express* **2013,** *6* (4), 043001.
20. Moorthy, M.; Palraj, J.; Kannan, L.; Katlakunta, S.; Perumal, S. Structural, microstructural, magnetic, and thermoelectric properties of bulk and nanostructured *n*-type $CuFeS_2$ Chalcopyrite. Ceram. Int. **2022**, 48, 29039-29048.
21. Moorthy, M.; Bhui, A.; Battabyal, M.; Perumal, S. Nanostructured $CuFeSe_2$ Eskebornite: An efficient thermoelectric material with ultra-low thermal conductivity. Mater. Sci. Eng. B **2022**, 284, 115914.
22. Bu, K.; Huang, J.; Luo, M.; Guan, M.; Zheng, C.; Pan, J.; Zhang, X.; Wang, S.; Zhao, W.; Shi, X.; Xu, L.; Huang, F. Observation of High Seebeck Coefficient and Low Thermal Conductivity in [SrO]-Intercalated $CuSbSe_2$ Compound. *Chem. Mater.* **2018**, *30* (16), 5539–5543.
23. Chen, T.; Ming, H.; Qin, X.; Zhu, C.; Huang, L.; Hou, Y.; Li, D.; Zhang, J.; Xin, H. Improving the Power Factor and Figure of Merit of *p*-Type $CuSbSe_2$ via introducing Sb Vacancies. *J. Mater. Chem. C* **2021**, *9*, 14858–14865.
24. Chen, T.; Ming, H.; Zhang, B.; Zhu, C.; Zhang, J.; Zhou, Q.; Li, D.; Xin, H.; Qin, X. Ultralow Thermal Conductivity and Enhanced Figure of Merit for $CuSbSe_2$ via Cd-Doping. *ACS Appl. Energy Mater.* **2021**, *4* (2), 1637–1643.
25. Temple, D. J.; Kehoe, A. B.; Allen, J. P.; Watson, G. W.; Scanlon, D. O. Geometry, electronic structure, and bonding in $CuMCh_2$ (M= Sb, Bi; Ch= S, Se): alternative solar cell absorber materials? *J. Phys. Chem. C* **2012**, 116 (13), 7334.
26. Li, D.; Qin, X. Y. Thermoelectric Properties of $CuSbSe_2$ and Its Doped Compounds by Ti and Pb at Low Temperatures from 5 to 310 K. *J. Appl. Phys.* **2006**, *100* (2), 023713.
27. Zhang, D.; Yang, J.; Jiang, Q.; Fu, L.; Xiao, Y.; Luo, Y.; Zhou, Z. Ternary $CuSbSe_2$ Chalcostibite: Facile Synthesis, Electronic-Structure, and Thermoelectric Performance Enhancement. *J. Mater. Chem. A* **2016**, *4* (11), 4188–4193.
28. Luo, Y.; Du, C.; Liang, Q.; Zheng, Y.; Zhu, B.; Hu, H.; Khor, K. A.; Xu, J.; Yan, Q.; Kanatzidis, M. G. Enhancement of Thermoelectric Performance in $CuSbSe_2$ Nanoplate-Based Pellets by Texture Engineering and Carrier Concentration Optimization. *Small* **2018**, *14* (50), 1–9.
29. Bode, B. M.; Gordon, M. S. MacMolPlt: A Graphical User Interface for GAMESS. *J. Mol. Graphics Modell.***1998**, *16* (3), 133–138.
30. Barca, G. M. J.; Bertoni, C.; Carrington, L.; Datta, D.; De Silva, N.; Deustua, J. E.; Fedorov, D. G.; Gour, J. R.; Gunina, A. O.; Guidez, E.; Harville, T.; Irle, S.; Ivanic, J.;

Kowalski, K.; Leang, S. S.; Li, H.; Li, W.; Lutz, J. J.; Magoulas, I.; Mato, J.; Mironov, V.; Nakata, H.; Pham, B. Q.; Piecuch, P.; Poole, D.; Pruitt, S. R.; Rendell, A. P.; Roskop, L. B.; Ruedenberg, K.; Sattasathuchana, T.; Schmidt, M. W.; Shen, J.; Slipchenko, L.; Sosonkina, M.; Sundriyal, V.; Tiwari, A.; Galvez Vallejo, J. L.; Westheimer, B.; Włoch, M.; Xu, P.; Zahariev, F.; Gordon, M. S. Recent Developments in the General Atomic and Molecular Electronic Structure System. *J. Chem. Phys.* **2020**, *152 (15)*, 154102.

31. Aroyo, M. I.; Perez-Mato, J. M.; Capillas, C.; Kroumova, E.; Ivantchev, S.; Madariaga, G.; Kirov, A.; Wondratschek, H. Bilbao Crystallographic Server: I. Databases and Crystallographic Computing Programs. *Zeitschrift fur Krist.* **2006**, *221* (1), 15–27.
32. Samanta, K.; Gupta, N.; Kaur, H.; Sharma, L.; Dogra Pandey, S.; Singh, J.; Senguttuvan, T. D.; Dilawar Sharma, N.; Bandyopadhyay, A. K. Order–disorder transition and Fano-interference in thermoelectric Cu_3SbSe_3 nanoparticles. *Mater. Chem. Phys.* **2015**, 151**,** 99–104.
33. Yan, H.; Xiao, R.; Pei, Y.; Yang, K.; Li, B. Structural, Electrical and Optical Characteristics of $CuSbSe_2$ Films Prepared by Pulsed Laser Deposition and Magnetron Sputtering Processes. *J. Mater. Sci.: Mater. Electron*. **2020**, *31* (1), 644–651.
34. Zhang, Y.; Li, L.; Li, D.; Wang, Q. Large-Scale Synthesis of Single Crystalline $CuSb(S_xSe_{1-x})_2$ Nanosheets with Tunable Composition. *J. Phys. Chem. C.* **2015**, *119* (3), 1496–1499.
35. Maeda, T.; Wada, T. First-Principles Study of Electronic Structure of $CuSbS_2$ and $CuSbSe_2$ Photovoltaic Semiconductors. *Thin Solid Films.* **2015**, *582*, 401–407.
36. Kshirsagar, A. S.; Khanna, Pawan. K. Reaction Tailoring for Synthesis of Phase-Pure Nanocrystals of $AgInSe_2$, Cu_3 $SbSe_3$, and $CuSbSe_2$. *ChemistrySelect* **2018**, *3* (10), 2854–2866.
37. Morgan, W. E.; Stec, W. J.; Van Wazer, J. R. Inner-Orbital Binding-Energy Shifts of Antimony and Bismuth Compounds. *Inorg. Chem.* **1973**, *12* (4), 953–955.
38. Pederson, L. R. Two-Dimensional Chemical-State Plot for Lead Using XPS. *J. Electron Spectrosc. Relat. Phenom.* **1982**, *28* (2), 203–209.
39. Wu, D.; Zhao, L. D.; Hao, S.; Jiang, Q.; Zheng, F.; Doak, J. W.; Wu, H.; Chi, H.; Gelbstein, Y.; Uher, C.; Wolverton, C.; Kanatzidis, M.; He, J. Origin of the High Performance in GeTe-Based Thermoelectric Materials upon Bi_2Te_3 Doping. *J. Am. Chem. Soc.* **2014**, *136* (32), 11412–11419.
40. Perumal, S.; Roychowdhury, S.; Negi, D. S.; Datta, R.; Biswas, K. High Thermoelectric Performance and Enhanced Mechanical Stability of *p*-Type $Ge_{1-X}Sb_xTe$. *Chem. Mater.*

2015, *27* (20), 7171–7178.

41. Morelli, D. T.; Jovovic, V.; Heremans, J. P. Intrinsically Minimal Thermal Conductivity in Cubic I-V-VI_2 Semiconductors. *Phys. Rev. Lett.* **2008**, *101* (3), 035901.
42. Pan, Y.; Li, J. F. Thermoelectric Performance Enhancement in *n*-Type $Bi_2(TeSe)_3$ Alloys Owing to Nanoscale Inhomogeneity Combined with a Spark Plasma-Textured Microstructure. *NPG Asia Mater.* **2016**, *8* (6), e275–e275.
43. Callaway, J. Model for Lattice Thermal Conductivity at Low Temperatures. *Phys. Rev.* **1959**, *113* (4), 1046.
44. Zhu, B.; Huang, Z. Y.; Wang, X. Y.; Yu, Y.; Yang, L.; Gao, N.; Chen, Z. G.; Zu, F. Q. Attaining Ultrahigh Thermoelectric Performance of Direction-Solidified Bulk *n*-Type $Bi_2Te_{2.4}Se_{0.6}$ via Its Liquid State Treatment. *Nano Energy* **2017**, *42*, 8–16.
45. Liu, Z.; Zhang, Y.; Mao, J.; Gao, W.; Wang, Y.; Shuai, J.; Cai, W.; Sui, J.; Ren, Z. The Microscopic Origin of Low Thermal Conductivity for Enhanced Thermoelectric Performance of Yb Doped MgAgSb. *Acta Mater.* **2017**, *128*, 227–234.
46. Tritt,T. M. Thermal Conductivity: Theory, Properties, and Applications; Springer Science & Business Media, 2005.
47. Qiu, W.; Wu, L.; Ke, X.; Yang, J.; Zhang, W. Diverse Lattice Dynamics in Ternary Cu-Sb-Se Compounds. *Sci. Rep.* **2015**, *5 (1)*, 1–7.
48. Majsztrik, P. W.; Kirkham, M.; Garcia-Negron, V.; Lara-Curzio, E.; Skoug, E. J.; Morelli, D. T. Effect of Thermal Processing on the Microstructure and Composition of Cu–Sb–Se Compounds. *J. Mater. Sci.* **2013**, *48* (5), 2188–2198.
49. Guttmann, G. M.; Gelbstein, Y. Mechanical Properties of Thermoelectric Materials for Practical Applications. In Bringing Thermoelectricity into Reality; Patricia Aranguren., Ed.; IntechOpen: London, 2018; pp 63-80.
50. Peccerillo, E.; Durose, K. Copper–Antimony and Copper–Bismuth Chalcogenides—Research Opportunities and Review for Solar Photovoltaics. *MRS Energy & Sustainability* **2018**, *5*, E13
51. Feng, B.; Li, G.; Pan, Z.; Hou, Y.; Zhang, C.; Jiang, C.; Hu, J.; Xiang, Q.; Li, Y.; He, Z.; Fan, X. Effect of Ba and Pb Dual Doping on the Thermoelectric Properties of BiCuSeO Ceramics. *Mater. Lett.* **2018**, 217, 189–193.

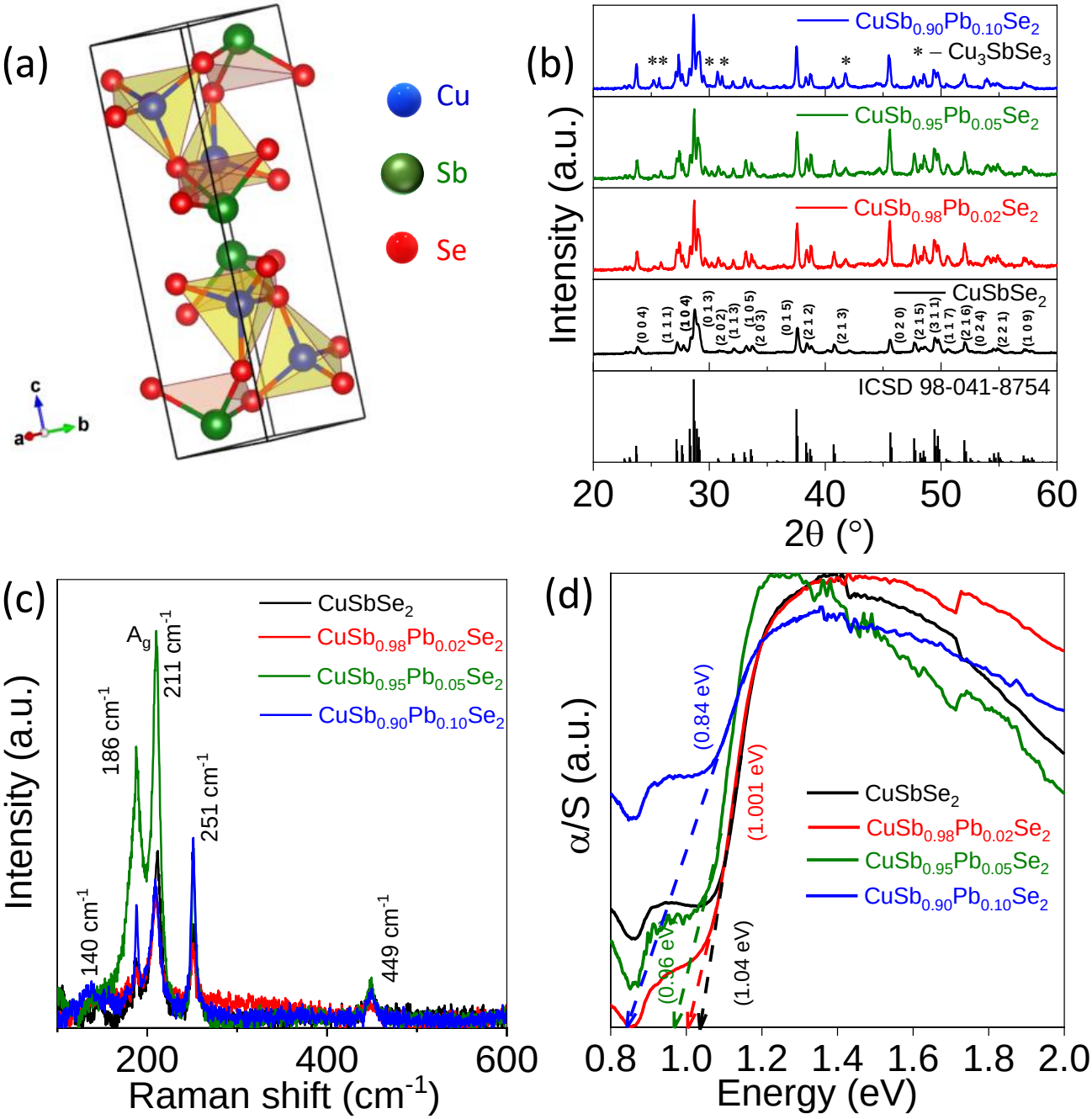

Figure 1. (a) Layered crystal structure of pure $CuSbSe_2$, (b) P-XRD patterns of $CuSb_{1-x}Pb_xSe_2$ (x = 0-0.10) powders, (c) Room temperature Raman spectra and (d) Optical absorption spectra of $CuSb_{1-x}Pb_xSe_2$ (x = 0-0.10) powders.

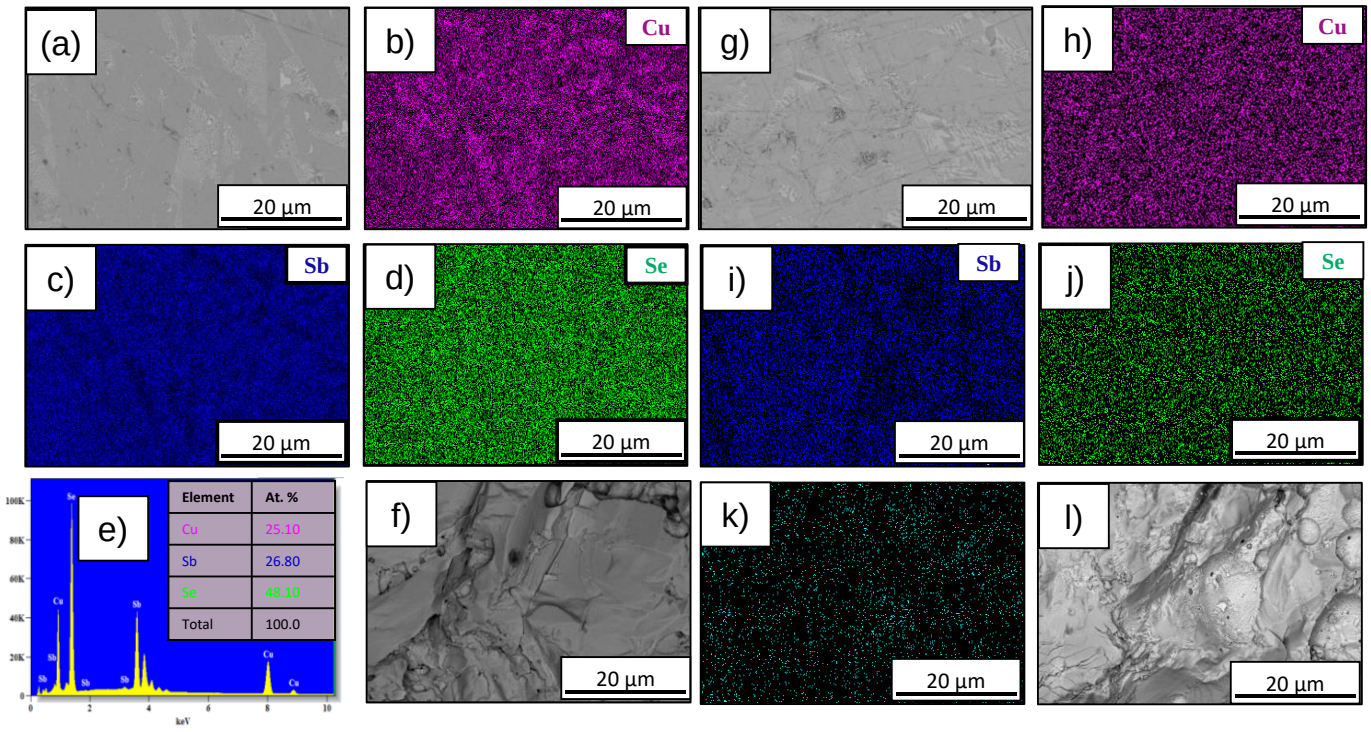

Figure 2. (a) BSE micrograph of polished $CuSbSe_2$ pellet, (b), (c), and (d) elemental mapping of Cu, Sb and Se, respectively. (e) and (f) are EDS spectra and fractograph of $CuSbSe_2$, respectively. BSE micrograph of polished $CuSb_{0.90}Pb_{0.10}Se_2$ pellet (g), elemental mapping of Cu, Sb, Pb, and Se, (h-k), respectively, and BSE fractured surface of $CuSb_{0.90}Pb_{0.10}Se_2$ (l).

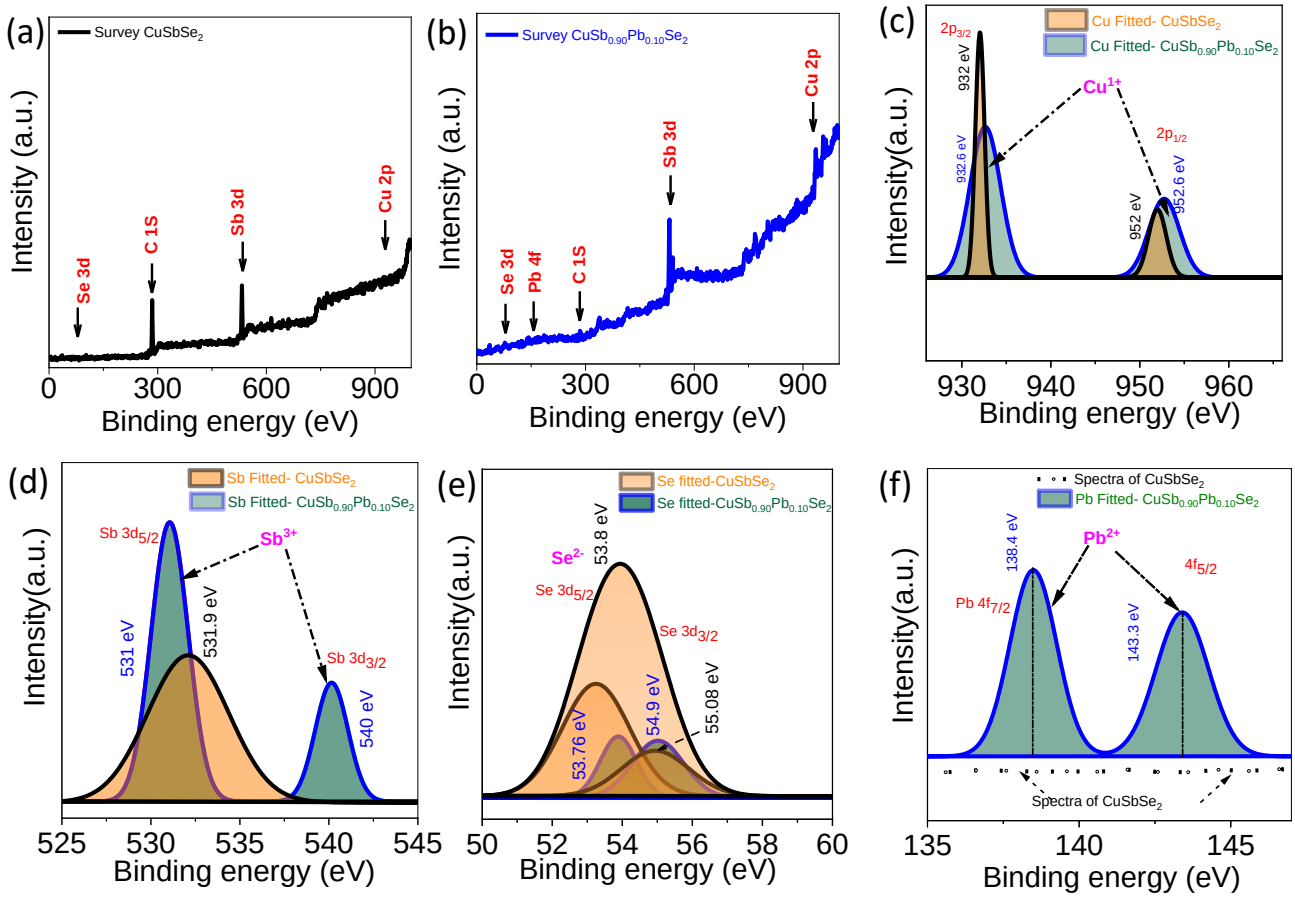

Figure 3. (a) Survey spectra of pure $CuSbSe_2$, (b) Survey spectra of $CuSb_{0.90}Pb_{0.10}Se_2$, (c) Cu core spectra, (d) Sb core spectra, (e) Se core spectra and (f) Pb core spectra of $CuSbSe_2$ and $CuSb_{0.90}Pb_{0.10}Se_2$.

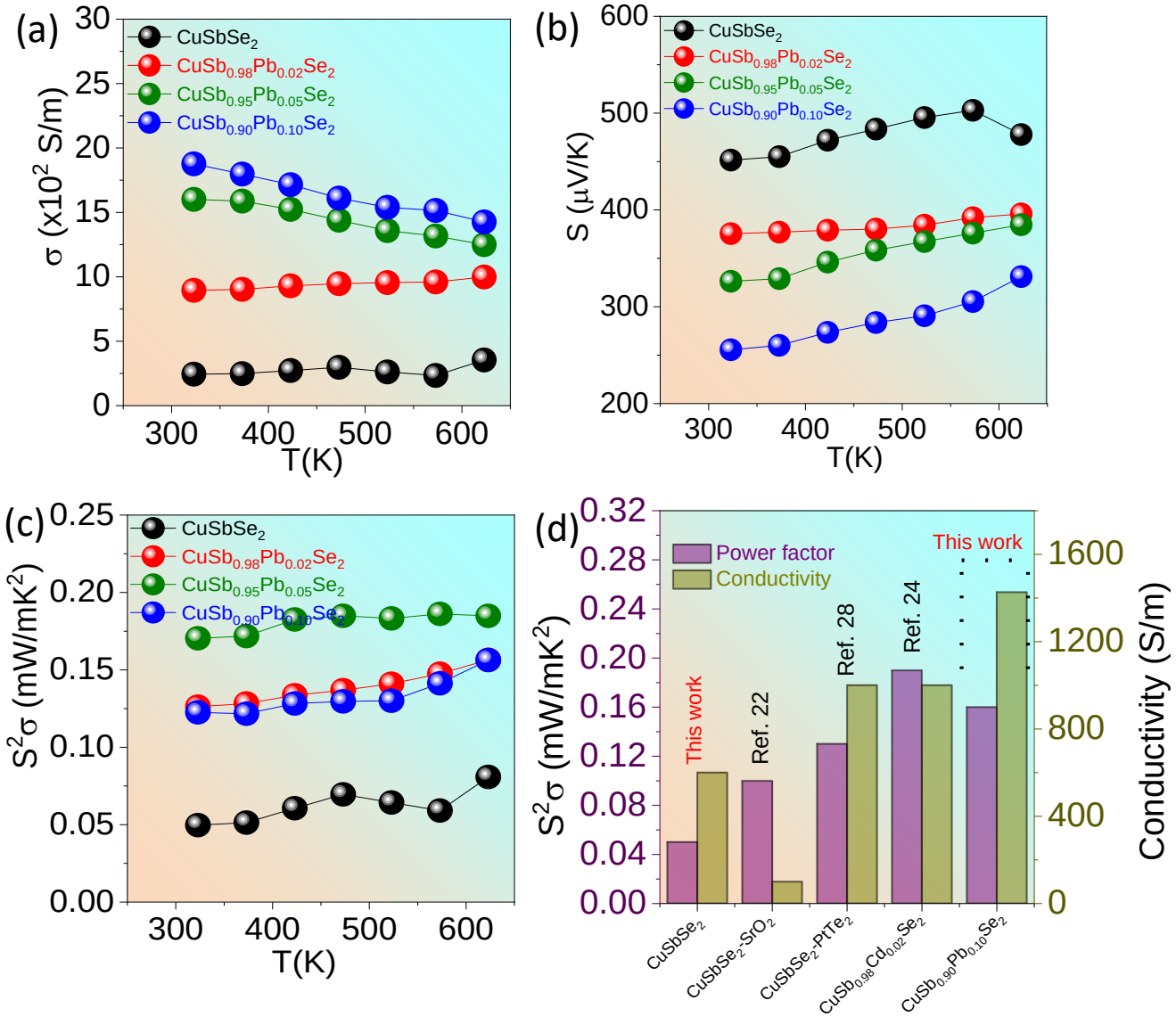

Figure 4. (a) Electrical conductivity (σ), (b) Seebeck coefficient (*S*), and (c) Power factor ($S^2\sigma$) of $CuSb_{1-x}Pb_xSe_2$ (x = 0-0.10) as a function of temperature and (d) Electrical conductivity (σ) and power factor ($S^2\sigma$) comparative bar chart with previous reports.[22, 24, 28]

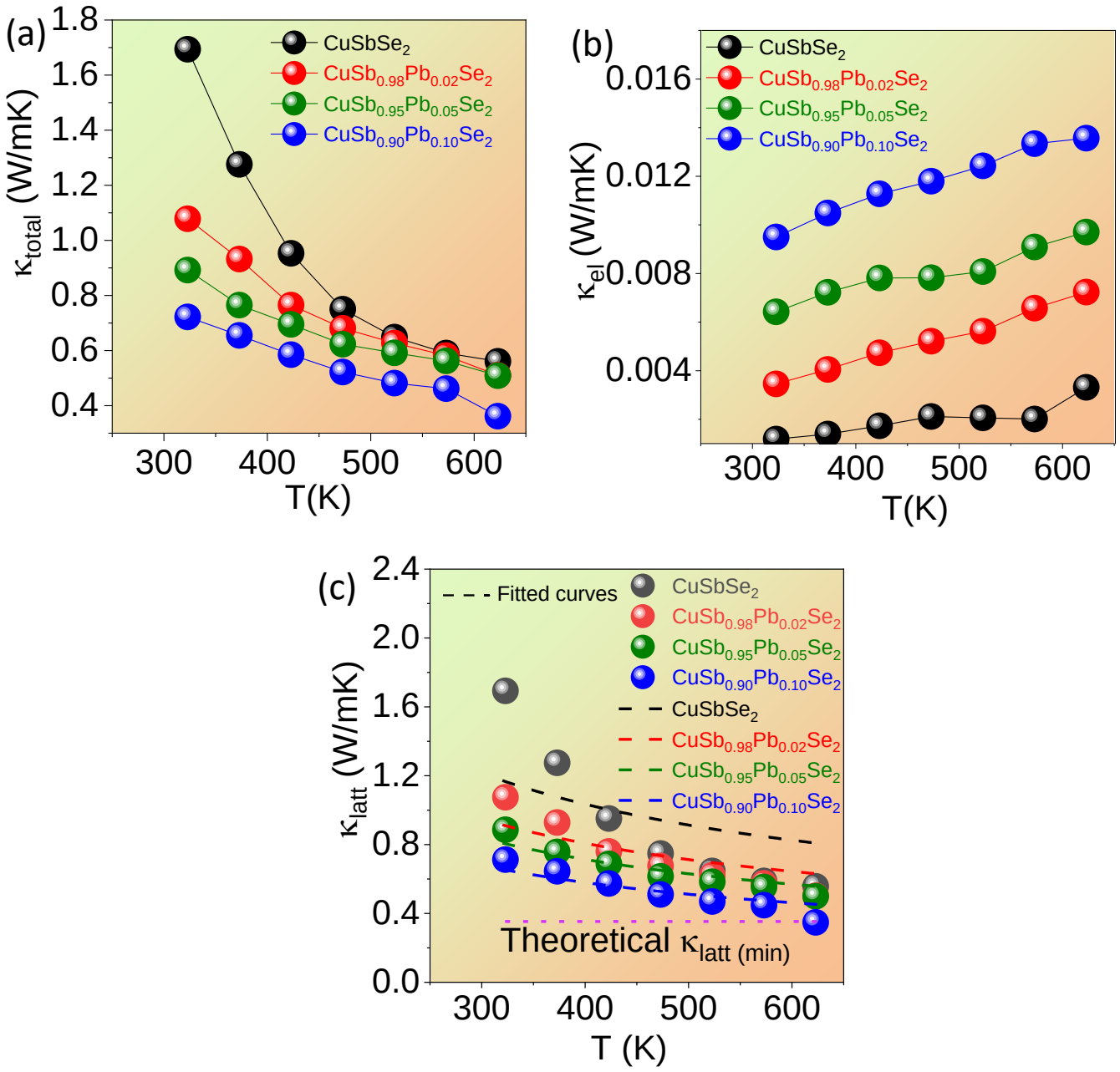

Figure 5. (a) Total thermal conductivity (κ_{total}), (b) Electronic thermal conductivity ($\kappa_{el.}$), and (c) Lattice thermal conductivity (κ_{latt}) of $CuSb_{1-x}Pb_xSe_2$ (x = 0-0.10) as a function of temperature.

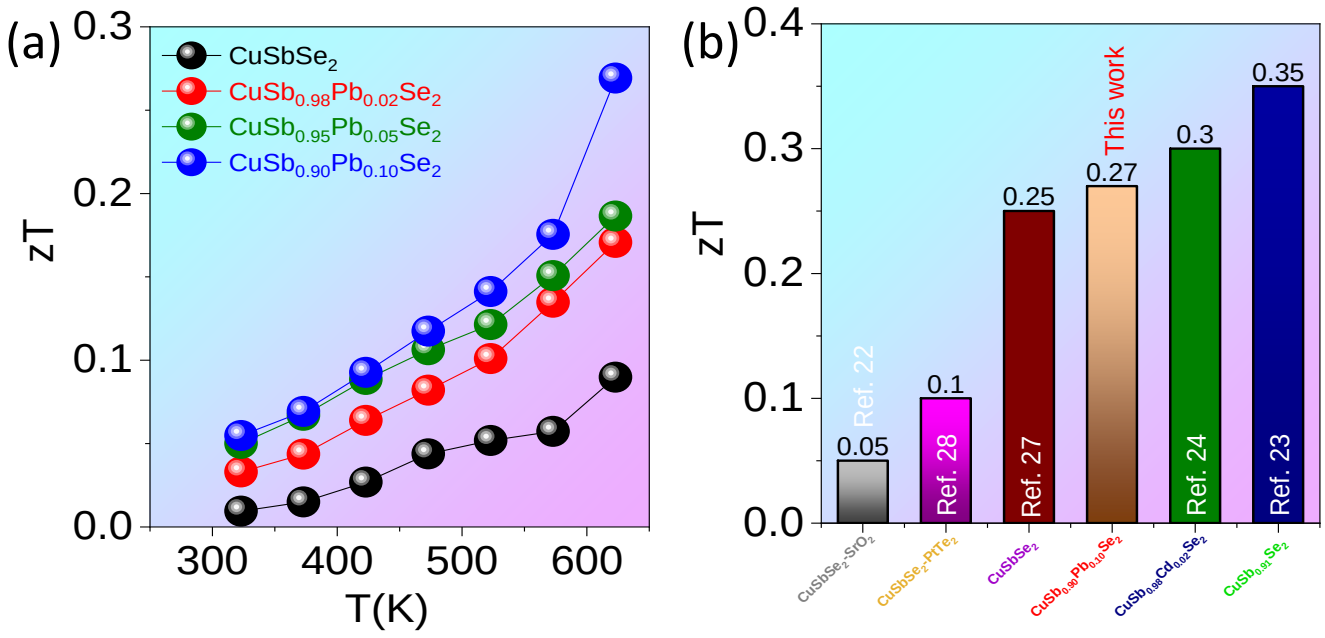

Figure 6. (a) Figure of merit, zT of $CuSb_{1-x}Pb_xSe_2$ (x=0-0.10) as a function of temperature and (b) Comparison plot of zT_{max} in the temperature range of 323-623 K with previous reports.[22, 23, 24, 27, 28]

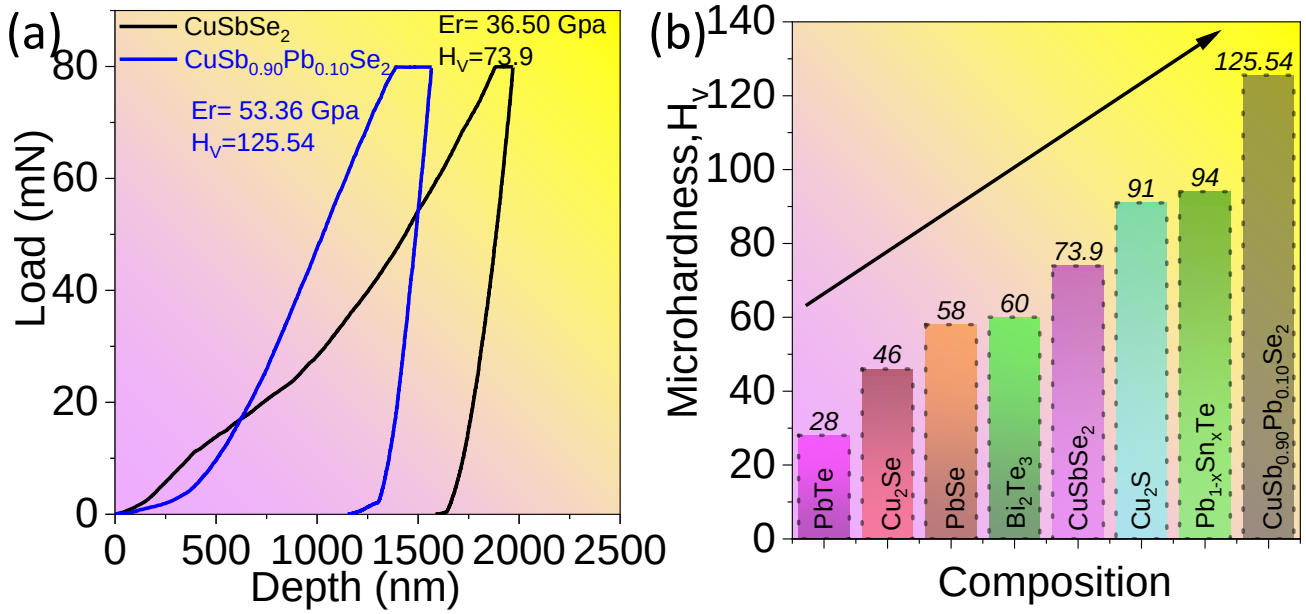

Figure 7. (a) The load vs. displacement curve for $CuSbSe_2$ and $CuSb_{0.90}Pb_{0.10}Se_2$; elastic modulus was calculated with reduced modules with a Poisson ratio of 0.30 and (b) micro-hardness (Hv) comparison with the state-of-the-art TE materials[48–51].

Table 1 provides density (d), the relative density (R_d), lattice parameters, lattice thermal conductivity scattering parameters (calculated with (θ_D= 56 K))- A (Umklapp) and B (point defect) of $CuSb_{1-x}Pb_xSe_2$

Composition	d (g/cm^3) (R_d)	Lattice parameter (Å)			A ($x10^{-38}$ s^3)	B ($x10^{-20}$ s/K)
		a	b	c		
$CuSbSe_2$	5.45 (92.6%)	6.2965(2)	3.9755(3)	14.9675(5)	3.88	2.59
$CuSb_{0.98}Pb_{0.02}Se_2$	5.43 (92.3%)	6.2971(4)	3.9801(2)	14.9808(2)	5.02	3.29
$CuSb_{0.95}Pb_{0.05}Se_2$	5.56 (94.5%)	6.3039(1)	3.9837(5)	14.9959(2)	5.64	3.74
$CuSb_{0.90}Pb_{0.10}Se_2$	5.49 (93.3%)	6.3073(7)	3.9863(2)	15.0119(4)	7.14	4.51

Table 2 summarizes the carrier concentration (n_p), electrical conductivity (σ), Seebeck coefficient (S), total thermal conductivity (κ_{total}), and thermoelectric figure of merit (zT) of $CuSb_{1-x}Pb_xSe_2$ (x = 0.00, 0.02, 0.05, and 0.10) samples.

Composition	n_p ($x10^{18}/cm^3$)	S (μV/K)	σ (S/m)	κ_{total} (W/mK)	zT$_{max}$
$CuSbSe_2$	1.12	478	354	0.56	0.09
$CuSb_{0.98}Pb_{0.02}Se_2$	2.23	425	770	0.51	0.17
$CuSb_{0.95}Pb_{0.05}Se_2$	5.86	384	1029	0.50	0.19
$CuSb_{0.90}Pb_{0.10}Se_2$	16.7	331	1426	0.36	0.27

Graphical abstract:

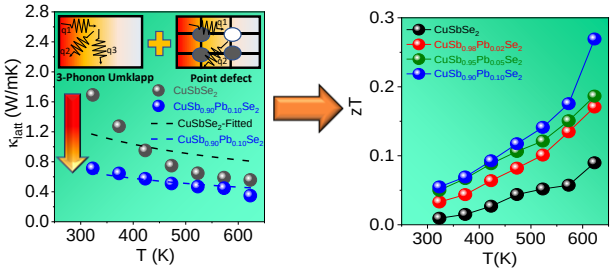

Illustration of lattice thermal conductivity reduction *via* phonon scattering from mass-fluctuations and point defects to improved *z*T in $CuSb_{1-x}Pb_xSe_2$ (x = 0-0.10) samples.